# Development of a Deployable Orbital Radio assembly (DORY) for VHF & AIS applications

P. Droste<sup>1</sup>, T.J. Fux<sup>2</sup>, L. Hennige<sup>2</sup>, L.T.A. Noll<sup>2</sup>, and M. Stempfle<sup>1</sup>

<sup>1</sup>SeeSat e.V.



### **Abstract**

Current estimates suggest that between 31% and 50% of the global fish production originates from illegal sources, amounting to approximately 11 to 26 million tons of fish per year [1]. This illegal practice of fishing is a strong both ecological and economical hazard. To combat these illegal fishing practices, vessel position signals such as those of the Automatic Identification System (AIS) can be monitored to locate misuse of fish resources. In the context of this work, a preliminary design of a stowable AIS antenna for a cubesat is investigated. The necessary antenna performance is determined with a link budget, with results indicating a required antenna gain  $G_R = 13.28[dBi]$  at an orbital altitude of h = 600[km]. Both a helical and a dipole design were considered in a preliminary analysis step, with the dipole antenna being chosen as the more suitable candidate. For the mechanical design of the antenna, a coiled tapespring boom was chosen, with four of these booms being stowed in a volume of approximately 0.4U. To inform the mechanical design, parametric studies investigating the influence of material choice on both the structural dynamics of the deployed boom and the deployment dynamics of the stowed boom are carried out. The influence of several geometric tapespring parameters on the boom dynamics was also investigated. Finally, the preliminary mechanical design of the antenna was simulated to check its functional performance, with a maximum antenna gain  $G_R = 2.39$  [dBi] and a return loss of approximately  $S \approx -15$  [dBi] being obtained. These results provide a baseline for future, more detailed investigations of the concept.

#### 1 Introduction

Illegal, Unreported, and Unregulated (IUU) fishing refers to fishing activities conducted by vessels and crews that do not comply with the legal, economic, or environmental regulations of the respective fishing areas [2]. IUU fishing poses a significant threat to marine ecosystems and local economies, particularly due to the involvement of highly industrialized foreign fleets [2]. Estimates suggest that between 31% and 50% of the global fish production originates from illegal sources, amounting to approximately 11 to 26 million tons of fish per year [1]. The market value of illegal fishing in Europe alone is estimated at around 1.1 billion euros [3].

Monitoring these illegal activities is challenging due to the vast areas that need to be observed and the ability of those involved to disable transponder systems such as AIS or VMS to avoid detection [1]. While satellite technology is already being used to monitor IUU activities, most estimates rely on data analyses conducted by Non-Governmental Organizations (NGOs) [4]. Integrated and dedicated payloads specifically for monitoring IUU fishing are rare. An example of innovative usage is the "Night Lights"

data product from the Skylight project, which leverages publicly available satellite data and analyzes nighttime imagery to identify vessel movements [5].

Despite the deactivation of transponder systems, optical identification of vessels using satellite technology remains possible. This technology has proven effective in other missions, particularly through the reception of AIS signals in Low Earth Orbit (LEO) to monitor vessel traffic even in remote regions [6]. A concrete example is the monitoring of shipping traffic along the Norwegian coast using a constellation of small satellites [7].

## 2 Preliminary Link Budget

In this study, the link budget for the DORY AIS antenna is calculated to determine the necessary gain required for the receiving antenna. The calculation assumes the transmission is solely affected by free space path loss, as atmospheric losses are negligible at the AIS frequency of 160 MHz. The satellite is assumed to be on the equatorial plane, and the transmitting antenna on the ship is modeled as a  $\lambda/2$  dipole antenna in free space, oriented vertically.

CC BY-SA 4.0 doi: 10.25967/630474

<sup>&</sup>lt;sup>2</sup>DHBW Ravensburg

The Link Budget calculation utilizes the Friis transmission equation, which has been rearranged to solve for the required gain of the receiving antenna,  $G_R$ . The equation considers the transmitted power  $P_T$ , the gain of the transmitting antenna  $G_T$ , and the distance R between the satellite and the transmitting source. The calculation explores how the required receiving antenna gain varies with the angle  $\theta$  between the satellite and the ship.

For different satellite altitudes ranging from 350 km to 600 km, and considering the AIS Classes A and B, the optimal angle  $\theta$  and corresponding minimum receiving antenna gain  $G_R$  were calculated. The results showed that as the altitude increases, the optimal angle decreases, and the required antenna gain increases. For instance, at an altitude of 350 km, the optimal angle  $\theta$  is 56.62°, with a required gain of -17.77 dBi for Class A and -9.81 dBi for Class B. At 600 km altitude, the optimal angle  $\theta$  reduces to 50.00°, and the required gains are -13.28 dBi and -5.32 dBi for Class A and B, respectively.

In Figure 1, the geometric relationship between  $\Theta$  and the transmission path is shown.

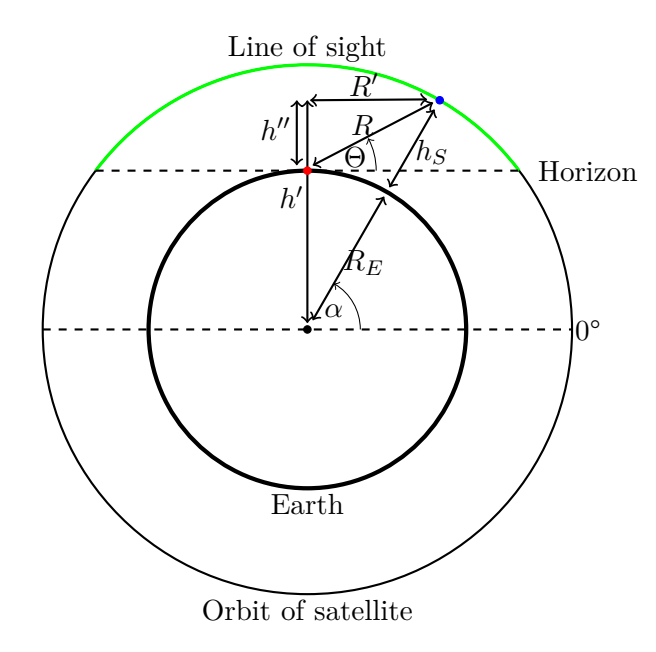


**Fig. 1:** Geometric Relationship for the Observation Angle

Using trigonometric functions, the following geometric relationships can be established:

$=\sin(\alpha)\cdot(R_E+h_s)\tag{1}$
$=\sin(\alpha)\cdot(R_E+h_s)$

$$h'' = h' - R_E \tag{2}$$

$$R' = \cos(\alpha) \cdot (R_E + h_s)$$

$$R = \sqrt{h''^2 + R'^2}$$

Altitude [km]	Gain $G_R$ [dBi]	
350	-17.77	
400	-16.67	
450	-15.70	
500	-14.82	
550	-14.02	
600	-13.28	

**Tab. 1:** Required Antenna Gain  $G_R$  (Class A) at Different Altitudes

Specification	Description
Receiving Frequency [MHz]	162
Min. antenna gain $G_{R,min}[dBi]$	-13.28
Max. operational angle $\Theta_{max}$ [deg]	80
Half-Power Beamwidth [deg]	60
Maximum return loss $S_{max}$ [dB]	-10

**Tab. 2:** Antenna Design Specifications for the DORY Satellite Mission

With the help of the Pythagorean theorem, the following formula for the transmission path can be derived. This path depends on the angle  $\alpha$ .

Equation 5 shows the dependency of the angle  $\Theta$  on the angle  $\alpha$ .

$$\Theta = \arctan 2 \left( h'', R' \right) \tag{5}$$

These results are summarized in table 1.

The performance specification for the receiving antenna was defined at an AIS standard frequency of 162 MHz, with the capability to achieve a gain of 2 dBi at an operational angle ( $\theta$ ) of 80°, in order to allow sufficient margin for potential operational deviations and future enhancements. Additionally, the half-power beam width was defined as 60°. To ensure high transmission efficiency and minimize signal loss, the antenna's input matching must result in a return loss better than -10 dB.

The design specifications for the antenna are summarized in table 2.

## 3 Preliminary Antenna Design

During the preliminary design phase for the DORY satellite's AIS antenna, various antenna types were

- assessed for feasibility. The helix antenna shows
- promise due to its simple design. Simulations for a Helix antenna were conducted with the parameters shown in table 3.

Parameter	Value
Angle	$37.5^{\circ}$
Conductor Diameter	$0.44\mathrm{cm}$
Spiral Diameter	$25\mathrm{cm}$
Spiral Offset	$2\mathrm{cm}$
Spiral Height	$73.4\mathrm{cm}$

**Tab. 3:** Parameters of the helix antenna with two spirals

At the target frequency of 162 MHz, the input reflection was found to be below -22 dB. Additionally, the antenna achieved a gain of 3 dBi in the primary radiation direction.

The final design decision focused on a dipole antenna, which provides balance between simplicity, performance, and compatibility with the CubeSat structure. The simulation was conducted with the parameters shown in table 4.

Parameter	Value	
Rod Diameter	$0.4\mathrm{cm}$	
Rod Length	$45.1\mathrm{cm}$	

Tab. 4: Parameters of the dipole antenna simulation

The dipole antenna achieved a return loss better than -15 dB and a directional gain of approximately 2.1 dBi, sufficient for the mission's requirements.

## 4 Mechanical Design

#### 4.1 Design Justification

As the CubeSat platform provides limited space for stowage of the antenna before deployment, several storage methods for the two dipole antennas were evaluated by collecting and combining the different options for antenna conductors, structure and stowage concepts before deployment. To keep the complexity of the mechanical design at a minimum thus reducing the probability for failure, a concept is opted for where the two dipole antennas are split into four antenna booms. Since the length of the individual booms is set to be 45.1 cm according to the conducted simulations in the previous section, the boom would have to be segmented when using a rigid antenna structure. To avoid such segmentations and the associated number of single points of failure, a flexible antenna concept was chosen, where the antenna booms have the shape of tapesprings and can therefore be rolled for optimized storage

space. With the particular shape of a tapespring, the booms require small forces to be rolled or unrolled while still maintaining a rigid form in the deployed stage. Additionally, they allow for controlled deployment and retraction, as discussed by T. W. Murphey et al. [8, 9] and J. Constantine et al. [10] for comparable concepts. To optimize storage space, all the antenna booms are rolled onto one coil, that is placed in the center of a 1 U CubeSat Segment with the booms being deployed to the four sides of the cube. Using this method, the length of the individual booms can be easily varied for other UHV applications by variing the diameter of the used coil in the center. The stowed antenna concept can be found in figure 2 and the deployed version in figure 3.

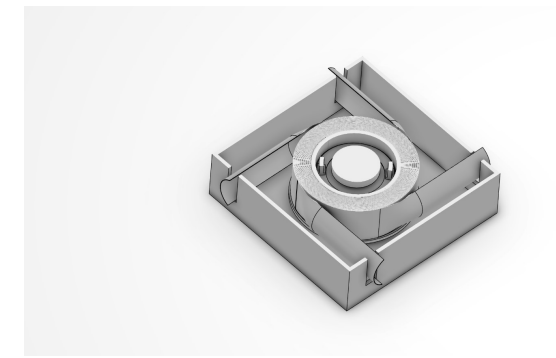


Fig. 2: Isometric view of the stowed antenna

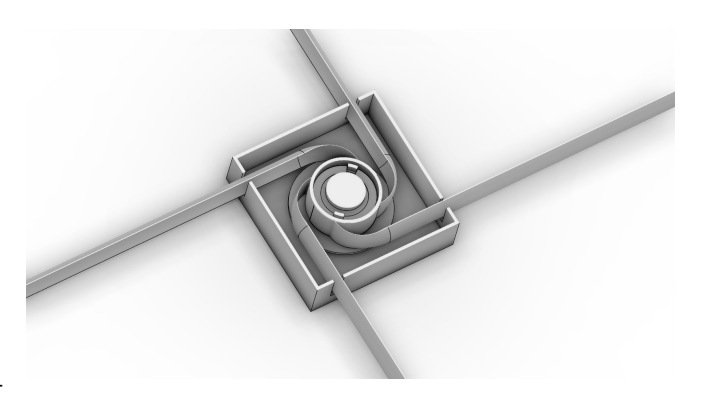


Fig. 3: Isometric view of the deployed antenna

The individual components of the assembled antenna design can be seen in the section view in figure 4. In this figure, some of the geometric parameters of the individual components are not yet to scale as their exact definition requires in depth analysis of various fields. The exact geometric parameters of the antenna booms are for example defined in section 5 according to an optimization process with the objective to minimize return loss for AIS signals. To aid in deployment and to be able to adjust the length of the antenna booms after their deployment, an electric motor (1) is installed which is connected

to the used reel (2) and mounted in a sleeve bearing (3). As a diameter for the motor 24 mm are provisionally assumed according to comparable motor types that are widely available. The inner diameter of the reel currently lies at 44 mm. To be able to transmit the signals detected by the antenna to the other subsystems of the satellite, a sliding contact (4) is used.

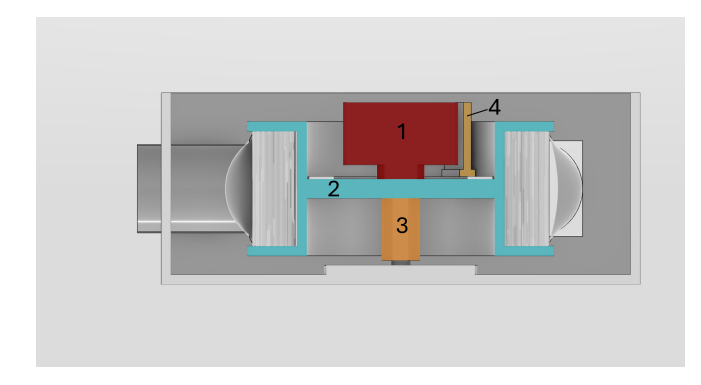


Fig. 4: Section view of the stowed antenna

Since there might be a possible scenario where the booms of the antenna are not entirely deployed, for example when shortening their individual length while adjusting the signal, the layering of the four booms on the reel could cause unwanted impedance and coupling effects between the signal components. For that reason, a second concept is investigated, where two antenna booms each are rolled up on a reel. With only two layers per reel, these effects can be reduced. The two reels are placed in opposite corners of the used segment an shown in figure 5. The individual structure of these subsystems is the same as for the single-reel concept show in figure 4. Both concepts are investigated in regard to their structural and deployment dynamics in the following sections.



**Fig. 5:** Isometric view of the stowed antenna on two coils

Material	$E_1$ GPa	$E_2$ GPa	$G_{12}$ GPa	ν <sub>12</sub> -	$\frac{\rho}{\rm kg/m^3}$
EN-AW7075	7	2	27	0.34	2800
17-4PH	200		77	0.30	7800
Ti6Al4V	1	14	43	0.32	4400
Toray T700 (Twill, 0.6FC)	69	69	1.4	0.06	1600
Toray T700 (Uni, 0.6FC)	138	3.9	1.4	0.3	1600
R glass fibre (Twill, 0.6FC)	28	28	1.4	0.06	2050

**Tab. 5:** List of properties for considered materials

#### 4.2 Material study

To inform the tapespring antenna design, the following analyses were carried out with respect to several different materials that are commonly in use for structural aerospace applications. The materials considered are listed along with their respective structural properties in table 5.

#### 4.3 Deployment dynamics

Studies conducted by previous authors have shown that a strain-energy-based approach may be used to calculate the forces present in the deployment dynamics of a stowable boom [8, 11, 12].

According to classical laminate theory, forces and moments on thin plates may be expressed as

$$\begin{bmatrix} \mathbf{N} \\ \mathbf{M} \end{bmatrix} = \begin{bmatrix} \mathbf{A} & \mathbf{B} \\ \mathbf{B} & \mathbf{D} \end{bmatrix} \cdot \begin{bmatrix} \boldsymbol{\epsilon} \\ \boldsymbol{\kappa} \end{bmatrix}$$
 (6)

where  $\mathbf{N} = [N_x N_y N_{xy}]^T$ ,  $\mathbf{M} = [M_x M_y M_{xy}]^T$ ,  $\boldsymbol{\epsilon} = [\epsilon_x \epsilon_y \gamma_{xy}]^T$  and  $\boldsymbol{\kappa} = [\kappa_x \kappa_y \kappa_{xy}]^T$  denote force, moment, elongation and curvature vectors, respectively.  $\mathbf{A}$ ,  $\mathbf{B}$  and  $\mathbf{D}$  denote the 3x3 stiffness coupling matrices [13].

Applying the properties of a symmetric, balanced laminate (or an isotropic material),  $\bf B$  vanishes. For a symmetric tapespring, no pure stretching contributions to the strain energy are present. Therefore the strain energy density per unit length in the x-direction and y-direction may be calculated as

$$\left[ \frac{d^2 U}{dx dy} \right]_{L} = \frac{1}{2} \cdot \boldsymbol{\kappa}^T \cdot \mathbf{D} \cdot \boldsymbol{\kappa} \tag{7}$$

$$= \frac{1}{2} \cdot \begin{bmatrix} \kappa_x \, \kappa_y \end{bmatrix} \cdot \begin{bmatrix} D_{11} & D_{12} \\ D_{12} & D_{22} \end{bmatrix} \cdot \begin{bmatrix} \kappa_x \\ \kappa_y \end{bmatrix} \quad (8)$$

which includes only the bending contributions to the strain energy [14].

As described in [11, 12], the stowed boom is affected by a torque consisting of four main contributions. First, the boom is affected by the bending energy stored within. Due to the energy state being at a non-equilibrium point for most orthotropic materials, a torque  $T_d$  that would deploy the boom into its undeformed state by converting the bending energy into kinetic energy is created. If this deployment is blocked, the coiled boom instead expands to a larger radius, thereby reducing curvature along the boom and by extension the stored bending energy. This process is referred to as blooming and is one of the most important failure modes of a tape-spring boom [11] since the boom is no longer correctly deployed. This expansion is created by a circular motion of the coiled boom which in turn is caused by a torque  $T_b$ . To avoid blooming, the boom is most often kept in shape by compression springs. The compression of these springs is another contribution to the energy balance and can be expressed as a virtual torque  $T_s$ . Finally, the layers of the coiled boom are also affected by the friction between adjacent layers, which may be expressed as a friction torque  $T_f$ . The sum of these torques may be expressed as

$$T = \frac{d}{d\theta_h} \left( E_d + E_b + E_s + E_f \right) \tag{9}$$

$$=T_d+T_b+T_s+T_f (10)$$

where E denotes the energy corresponding to each of the previously described contributions and  $d/d\theta$  denotes the derivative with respect to the angle  $\theta_h$  traversed by the hub rotation.

The contributions may be calculated through

$$T_d(\theta_h) = (R_r + a(\theta_c - \theta_h)) \cdot b \cdot \left[ \frac{d^2 U}{dx dy} \right]_b$$
 (11)

$$T_b(\theta_h) = \frac{d}{d\theta_h} \int_0^{\theta_c - \theta_h} (R_b + a\theta) \cdot b \cdot \left[ \frac{d^2 U}{dx dy} \right]_b d\theta \quad (12)$$

$$T_s(\theta_h) = -n_s \cdot F_s(\theta_h) \cdot \frac{ds}{d\theta_h} \tag{13}$$

$$T_f(\theta_h) = \mu \cdot N(F_s) \cdot \frac{dl_c}{d\theta_h}$$
(14)

where  $R_r$  and  $R_b$  are the reel radius and the inner blooming coil radius, b is the tapespring arc transverse arc length,  $l_c$  is the contacting length of the tapesprings and  $a = n_t t/2\pi$  denotes the pitch of the

Parameter	Setting
Mesh element shape Mesh element type Mesh element size	Quadrilateral S4 shell section 1 [mm]

Tab. 6: FEM model parameters

coiled tapespring.  $F_s(\theta_h)$  is the force exacted by each spring due to the deformation s, while  $N(F_s)$  is the total force resulting from friction between coil layers. The latter is determined semi-empirically [11] through

$$N = 2(n_c - 1)^{0.7} \cdot \left(F_s + 1.2bD_{11}\kappa_y^2\right) \tag{15}$$

Using these expressions, the total torque exacted by the tapesprings can be plotted over the traversed hub angle. If there is an obstacle to the tapespring that provides sufficient reaction force to stop the deployment against the tapespring torque, the boom is instead forced to expand inside the housing, i.e. blooming occurs.

Figure 6 shows the torque exhibited by the boom onto the spindle and the generated tip force for a blooming boom. The assembly was assumed to include four spring with a preload of  $F_s = 3$  [N] each. These torque values do not include friction torque. The magnitude of friction torque lies in a range between  $T_f = -1$  [Nm] and  $T_f = -2$  [Nm] over the entire deployment sequence of the boom. As such, it would exceed the torque provided by the three other constituents, resulting a stationary boom.

However, all results for deployment of the boom need to be verified through tests, since it is not clear whether the semi-empirical relations hold for the present boom design featuring four tapespring booms on a single reel.

### 4.4 Boom Structural Dynamics

To inform the material selection for the boom design, the influence of geometry and material properties on the fundamental frequencies of the fully deployed boom was investigated. For this, a parametric FEM model was constructed and a modal analysis on the deployed boom structure carried out. The Abaqus implementation of 3DEXPERIENCE~R2024~RD03 was used for solving the FEM system. The respective model parameters are given in table 6.

The results of the finite element simulations are shown in figures 7, 8 and 9. Several mode shapes

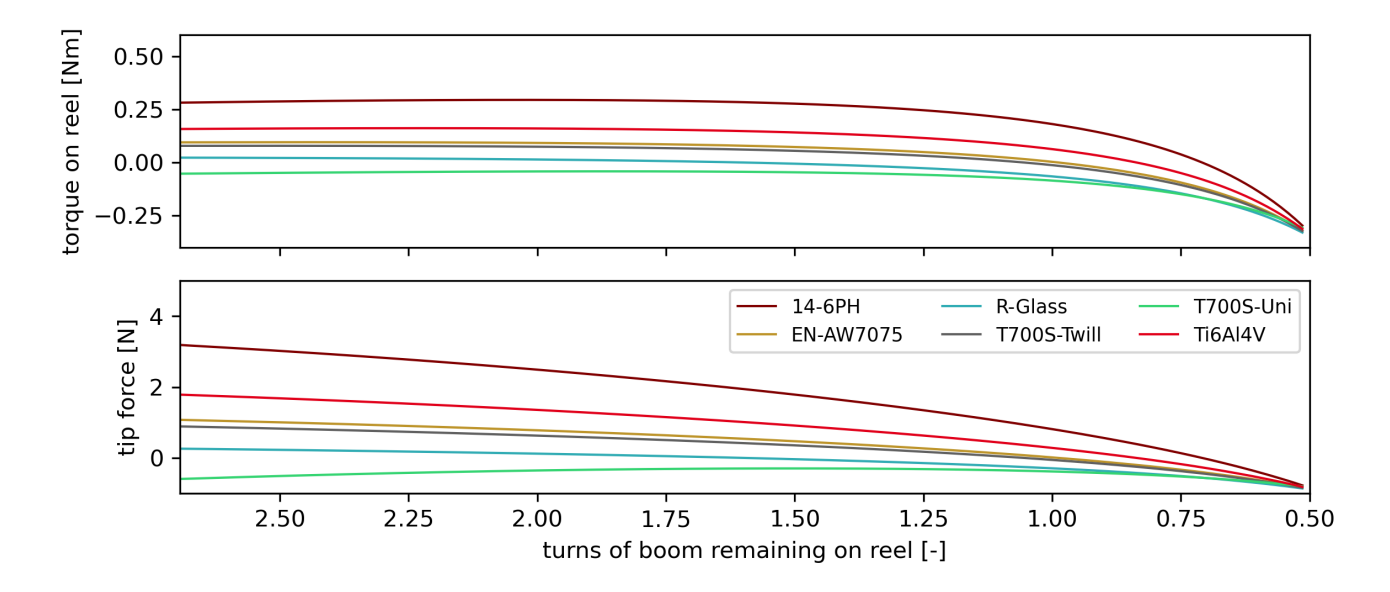


**Fig. 6:** Torque  $T_t$  and tip force  $F_{tip}$  for a blooming boom in configuration 1

Parameter	$t [\mathrm{mm}]$	r [mm]	$\phi$ [deg]	$l \; [\mathrm{mm}]$
Value	0.125	12	135	380

Tab. 7: Tapespring baseline design parameters

were present in the first three fundamental modes of each simulated boom. Figure 7 gives an overview of these mode shapes.

The results of varying the materials of the basic boom defined by the parameters in table 7 are shown in figure 8. As is apparent, all three of the considered metals show similar results, with the first three modes all exhibiting a first torsional, first bending, and second torsional mode shape, ordered from lowest to highest fundamental frequency. Additionally, the frequency of each fundamental mode is virtually the same for all three materials. This is likely a result of the fact that the chosen metals have very similar specific elastic and shear moduli  $E/\rho$  and  $G/\rho$ . For a bending beam with constant geometry, the simple fundamental mode frequencies are roughly directional proportional to these parameters which explains the similarity in fundamental modes.

Of the three selected composite materials, the two twill-weave materials exhibit the same order of mode shapes as the metallic materials. However, there are some strong differences in the frequencies at which the fundamental modes occur. While the metals have first torsional and first bending modes at very similar frequencies, composite twill materials show a much larger separation of these two modes. This is likely a result of the fact that the elasticity and shear moduli show a much larger relative difference

than is the case for the metallic booms. This separation is also the case for the unidirectional composite. However, the mode shapes occuring within the first three fundamental modes are very different from those of the remaining composite booms. While the first mode is still a basic first torsional mode, the second and third fundamental modes exhibit a coupled and transverse bending behaviour, respectively. The second mode behaviour is especially critical, since the transverse bending is similar to that encountered during buckling of the boom. As this mode may lead to structural failure or an uncontrollable oscillation of the antenna.

Summarizing, for the metal alloys investigated, there seems to be no clear advantage to either of these materials from a structural dynamics perspective. As such, emphasis can be placed on secondary characteristics of the materials, such as cost or ease of manufacturing. However, to fully confirm this, additional analysis needs to be performed to understand the effects of fatigue encountered during coiling and uncoiling of the boom. Additionally, the effect of material parameters on the deployment of the boom needs to be considered as well.

Results for the composite materials indicate that commonly available twill weave materials are also a suitable option for the boom design. Due to their the stronger frequency separation of the first and second modes, they also reduce the complexity of structural vibrations that need to be handled by the attitude control system of the respective cubesat. This may be an important fact when designing the overall cubesat system. The unidirectional composite has the advantage of providing the highest

bending stiffness of all considered materials which may be useful when designing a longer boom. For the antenna parameters considered here, however, the risk of failure and oscillation stemming from the coupled modes is judged to be too severe, however. As such, the T700S twill composite is used as a preliminary material choice for the remaining investigations of this work.

To allow for optimization of the antenna design, several modal analyses were carried out, varying the different geometric parameters of the boom tapespring. The results are shown in figure 9. Since the boom length l is the parameter that is most strongly dictated by the functional antenna design, structural design optimization can most easily be carried out using the remaining three parameters  $r_y$ ,  $\phi$  and t. Overall, nine configurations were investigated, with three values for the boom cross-section sector angle  $\phi$  and radius of curvature  $r_y$ , respectively. The boom cross-section thickness was not varied, since a substantial increase would likely be needed, leading to limitations in coiling the boom to its stowed state.

Since both  $\phi$  and  $r_y$  linearly influence the arc length of the boom cross-section and thereby the height of the stowed boom, it is of interested which of the parameters has a larger effect on the fundamental mode frequencies. To determine this influence, the relative change in frequency stemming with regard to the relative change in either  $r_y$  or  $\phi$  is calculated. The results are shown in tables 8 through 10.

Simulation results for the boom cross-sectional geometry indicate several facts about the tapespring structural dynamics. For one, the first torsional mode is affected to a lesser degree by increasing  $\phi$ and  $r_y$  than the two other modes are. This is likely a result of the fact that the tapespring presents an open cross-section which reduces the torsional stiffness gains to be made from increasing the size of the cross-section. It should also be noted, that the finite element results indicate a decrease in the first torsional fundamental frequency for some combinations of  $r_y$  and  $\phi$ , as can be seen in table 9. This effect is only present in one case for the second torsional mode (see table 10). Similarly, the relative increase in frequency is higher for the second torsional mode than it is for the first.

The change in the first bending fundamental frequency in contrast seems to be much more regular. While not completely linear, the rate of change with b and  $\phi$  seems to be largely independent of the other parameter. This is not the case for both torsional mode changes, where a change in  $r_y$  influences the change induced by  $\phi$ , and conversely.

Overall, it can be noted that a change in  $\phi$  seems to have a larger effect on the fundamental frequency than changes in  $r_y$  do. Therefore, in the design space investigated, increasing the sector angle  $\phi$  should be preferred to increasing the transverse radius of curvature of the tapespring as the former increases the deployed boom stiffness at a lower increase in height of the stowed tapespring. However, the influence of these parameters on the deployment of the boom should always be investigated, as well.

#### 5 Detailed antenna simulation

To investigate whether the mechanical design concepts described in the previous sections are feasible from a functional perspective, a new set of simulations were carried out. For these antennas, the antenna booms were modeled as straight tapesprings with the parameters shown in table 7.

The model used for the simulation is shown in figure 10. The tapesprings themselves were modelled as ideal conductors. To reduce model complexity, the cubesat was simplified to a fully closed, grounded volume. The antenna was set at the base surface of the cubesat while the opposite surface features four solar panels. The signal collected by each booms was combined into one common pick-up point. Antenna gain and return loss determined from this combined signal. This simplification assumes that there is no overlap between the booms after deployment and there is no significant coupling between the signal components transmitted through each boom resulting from the boom geometry. Additionally, the antenna internals were neglected for the simulation as they are assumed not to have a large impact on the receiving qualities of the antenna.

As can be gleaned from 11, increasing the radius of curvature has the effect of increasing return loss while at the same time reducing its rate of change with regard to the frequency. Similarly, the point of minimum return loss is shifted toward lower frequencies. These effects can likely be attributed to the fact that a lower radius of curvature at constant sector angle and boom length moves the boom geometry closer to an ideal rod.

In reality, the reduction in cross-section would likely have the additional effect of increasing impedance in the boom. This effect should be considered in subsequent simulations of the boom that factor in the electrical characteristics of the boom material. Overall, however, the return loss results indicate that boom cross-section can be adjusted based on the needs defined by mechanical constraints

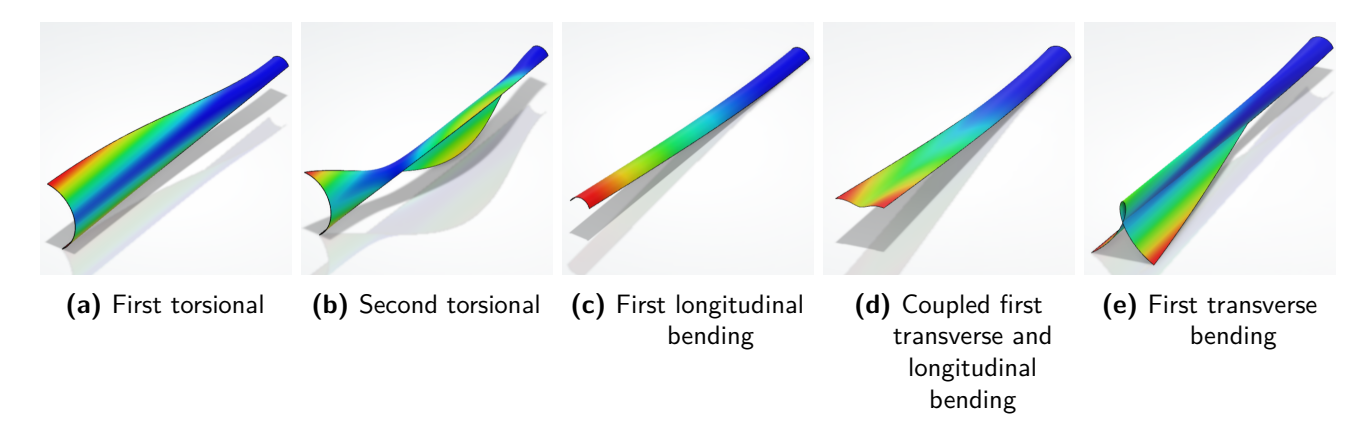


Fig. 7: Mode shapes encountered for boom dynamics

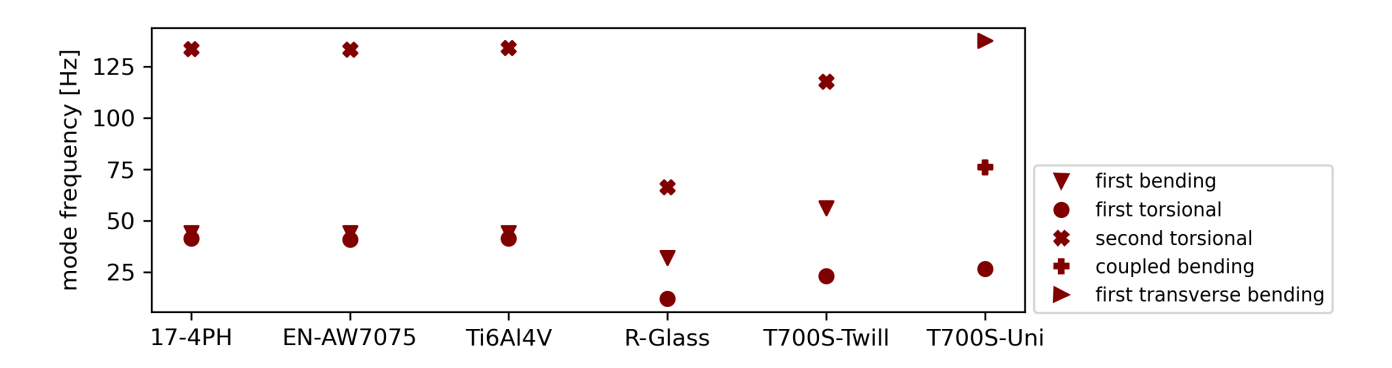


Fig. 8: First three fundamental modes for several boom materials

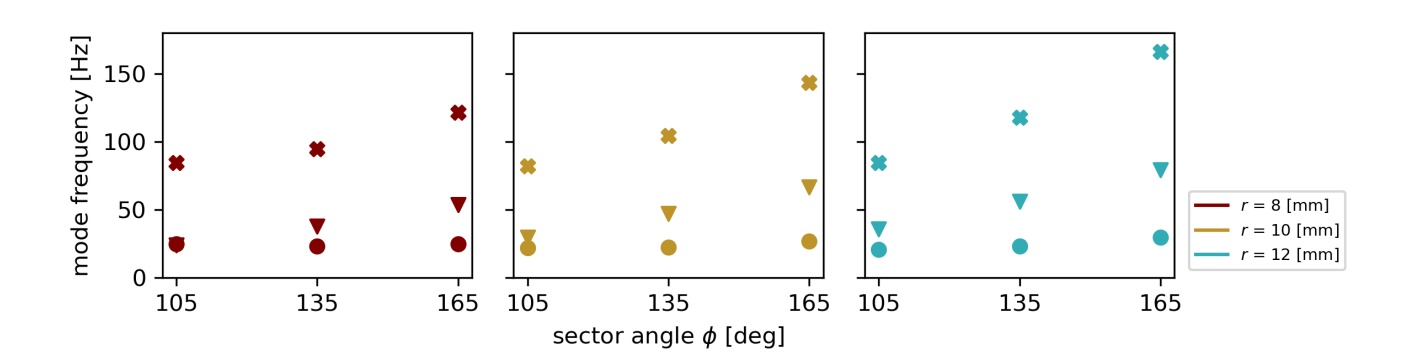


Fig. 9: First three fundamental modes for several boom cross-section geometries

$\Delta f_{b1,rel}/\Delta \phi_{rel}$	$\phi = 105 \deg$		$\phi = 135 \deg$		$\phi = 165 \deg$
r = 8  mm		2.05		1.86	
	0.99		0.98		0.97
r = 10  mm		2.04		1.85	
	0.99		0.96		0.96
r = 12  mm		2.02		1.85	

**Tab. 8:** Relative change in first bending fundamental frequency for changes in  $r_y$  and  $\phi$ 

$\Delta f_{t1,rel}/\Delta \phi_{rel}$	$\phi = 105 \deg$		$\phi = 135 \deg$		$\phi = 165 \deg$
r = 8  mm		-0.23		0.27	
	-0.43		-0.12		0.32
r = 10  mm		0.063		0.82	
	-0.34		0.13		0.58
r = 12  mm		0.42		1.28	

**Tab. 9:** Relative change in first torsional fundamental frequency for changes in  $r_y$  and  $\phi$ 

$\Delta f_{t2,rel}/\Delta \phi_{rel}$	$\phi = 105 \deg$		$\phi = 135 \deg$		$\phi = 165 \deg$
r = 8  mm		0.41		1.27	
	-0.12		0.42		0.72
r = 10  mm		0.95		1.67	
	0.15		0.64		0.79
r = 12  mm		1.37		1.84	

**Tab. 10:** Relative change in second torsional fundamental frequency for changes in  $r_y$  and  $\phi$ 

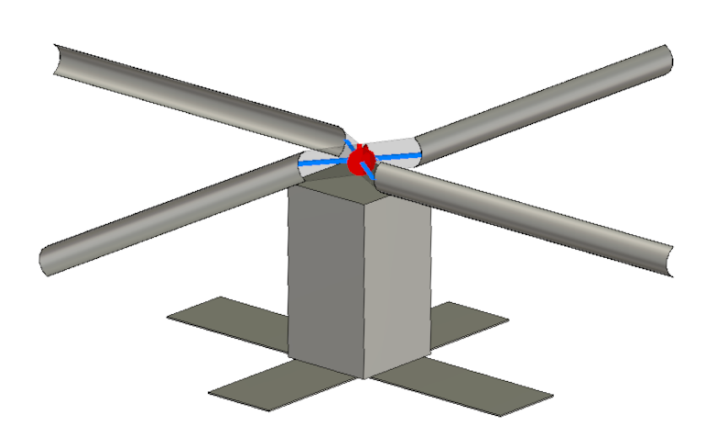


Fig. 10: Cubesat model used for antenna simulation

Parameter	Result
maximum antenna gain $G_{max}$ [dBi]	2.39
half-power beam width [deg]	79.2

**Tab. 11:** Main antenna gain results

without the impact on the functional parameters being too severe. If the design space is to be extended toward other radii of curvature, however, this assumption should be analysed in more depth.

The antenna gain provided by the antenna is very similar to that of an ideal dipole antenna with the directional antenna gain also conforming to expectation. Comparing the values from figure 12 to the antenna gain requirements defined in table 1, the antenna is able to fulfill the requirements for all signal up to a maximum angle of  $\Theta_{max} = 80$  deg from the maximum antenna gain direction.

#### 6 Conclusion

In the context of this work, a preliminary design of a stowable AIS antenna for a cubesat was investigated. The necessary antenna performance was determined with a link budget, resulting in a required antenna gain  $G_R = -13.28$  dBi at an orbital altitude of h = 600 km. Both a helical and a dipole design were considered in a preliminary design step, with the dipole antenna being chosen as the more suitable candidate. For the mechanical design of the antenna, a coiled tapespring boom was chosen. The accommodation of the tapespring booms inside a volume of approximately 0.4 U. To inform the mechanical design, parametric studies investigating the influence of material choice on both the structural dynamics of the deployed boom and the deployment dynamics of the stowed boom were carried out. The influence of several geometric tapespring parameters on the boom dynamics was also investigated. Finally, the preliminary mechanical design of the antenna was simulated to check its functional performance, with a maximum antenna gain  $G_R = 2.39$  dBi and a return loss of approximately  $S \approx -15$  dB being obtained. The current design state shows promise with regard to its applicability for measuring AIS signals but needs to be supplemented with further analysis before a design baseline can be firmly established.

#### References

[1] The State of World Fisheries and Aquaculture 2020: Sustainability in Action. Rome: Food and Agriculture Organization of the United

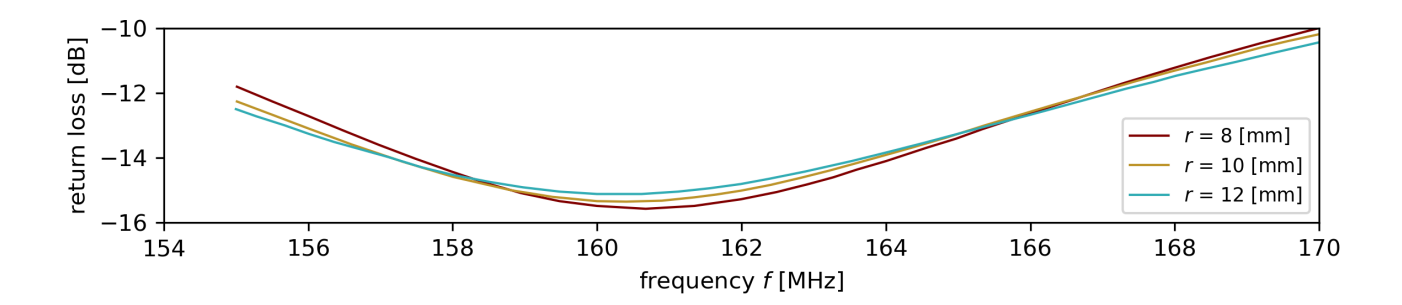
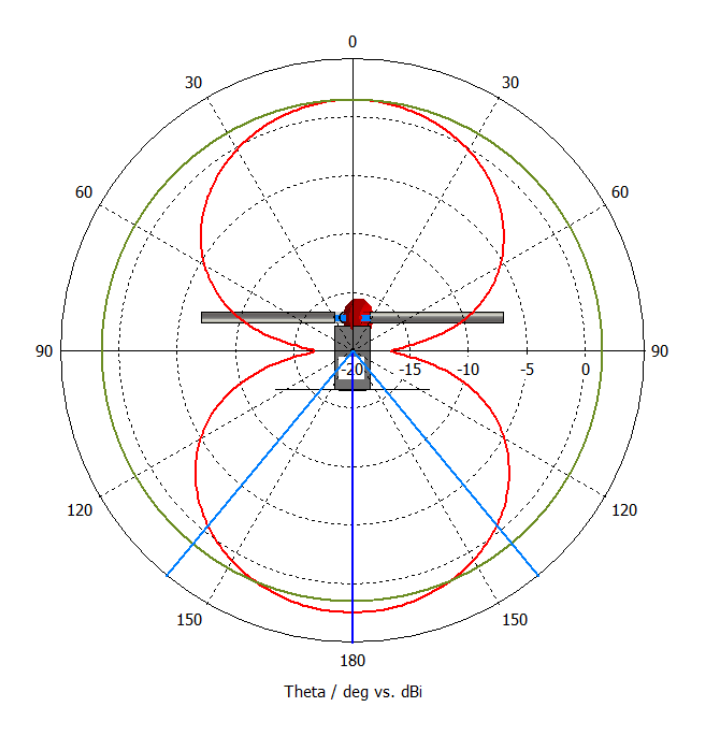


Fig. 11: Return loss for several tapespring radii of curvature



**Fig. 12:** Directional antenna gain at f = 162 MHz

Nations (FAO), 2020. DOI: 10.4060/ca9229e n.

- [2] David J. Agnew et al. "Estimating the Worldwide Extent of Illegal Fishing". In: *PLoS ONE* 4.2 (2009), e4570. DOI: 10.1371/journal.po ne.0004570.
- [3] European Commission. The EU Fish Market 2020 Edition. Luxembourg: Publications Office of the European Union, 2020.
- [4] Eyes on the Seas. Washington, D.C.: Pew Charitable Trusts, 2015.
- [5] SkyTruth. Skylight: A Satellite-Based Maritime Monitoring System. Shepherdstown, WV: SkyTruth, 2020.
- [6] Space Norway. Norwegian AIS Satellite System (NorSat). Oslo, Norway: Space Norway, 2022.

- [7] Jon Harr et al. "Microsatellites for Maritime Surveillance - an update on the Norwegian Smallsat Program". In: Oct. 2018.
- [8] T. W. Murphey and S. Pellegrino. "A novel actuated composite tape-spring for deployable structures". In: Collection of Technical Papers AIAA/ASME/ASCE/AHS/ASC Structures, Structural Dynamics and Materials Conference 1 (2004), pages 260–270. DOI: 10.2514/6.200 4–1528.
- [9] T. W. Murphey et al. "Deployable booms and antennas using Bi-stable tape-springs". In: Proc. 24th AIAA/USU Conf. Small Satell. SSC10-X-6. Logan, Utah, 2010.
- [10] Joseph Constantine et al. "CubeSat Deployable Antenna Using Bistable Composite Tape-Springs". In: *IEEE Antennas and Wireless Propagation Letters* 11 (2012), pages 285–288.
- [11] S. Wang et al. "Tip force and pressure distribution analysis of a deployable boom during blossoming". In: International Journal of Solids and Structures 193-194 (June 2020), pages 141–151. DOI: 10.1016/J.IJSOLSTR.2 020.01.026.
- [12] Sicong Wang et al. "Driving Force and Blossoming Analysis of a Composite Triangular Rollable and Collapsible (TRAC) Boom Used in Aerospace Technologies". In: *Aerospace* 2024 11 (4 Apr. 2024), page 311. DOI: 10.339 0/AEROSPACE11040311.
- [13] A. T. Nettles. Basic Mechanics of Laminated Composite Plates. NASA Reference Publication NASA-RP-1351. NASA Marshall Space Flight Center, Oct. 1994.
- [14] E. H. Mansfield. *The Bending and Stretching of Plates*. 2nd Edition. Cambridge University Press, 1989.